Abel Inversion of Emission and Backlighting Images

The Abel inversion is used to calculate local plasma quantities (in three dimensions) from line-of-sight measurements. Two examples relevant to laser-driven implosion experiments are the imaging of x-ray radiation where (a) the Abel inversion of emission images yields the local emission, and (b) the Abel inversion of backlit images yields the local density. As explained below, the imaging in the first case can be either two-dimensional or one-dimensional, but in the second case it must be two-dimensional. For x-ray emission, the Abel inversion procedure can be complicated by self-absorption within the emitting volume (in addition to attenuation by the surrounding shell). However, in the case of backlighting images, the problem is simpler because absorption occurs mostly in the colder parts of the compressed target, where emission can be negligibly small. In the case of imploding cryogenic targets, the situation is further simplified because (a) the compressed core consists of only hydrogenic ions, and (b) the absorbing layer is spatially separate from a central emitting hot spot. We therefore choose cryogenic implosions to demonstrate the utility of the Abel-inversion procedure applied to both two-dimensional and one-dimensional x-ray images. We use target profiles calculated by *LILAC* to simulate experimental images by applying a simplified radiation transport model, then analyze them through the Abel inversion and compare the results to the original target parameters.

Monochromatic images are required for the analysis presented here because of the wavelength dependence of the employed parameters (opacity and continuum emission). Additionally, in the case of backlighting, monochromatic images help discriminate the backlighting image against the target self-emission.[1,2] Two-dimensional monochromatic images can be achieved with an x-ray microscope fitted with a diffracting crystal between the optics and the image plane—a method recently developed at LLE by F. J. Marshall. Spatial resolution in the 8- to 12-μm range has been experimentally demonstrated.[3] One-dimensional polychromatic imaging can be obtained with a crystal spectrograph equipped with a resolving slit. We will assume that a spatial resolution of 10-μm FWHM can be achieved in either case.

The intensity emitted by the target is a line integral of the local emission and can therefore be Abel-inverted. In the case of backlighting, it is the opacity, rather than the measured intensity, that can be Abel-inverted. In two-dimensional imaging of a backlit target, each image point yields the opacity along the corresponding line of sight, and the opacity image can thus be Abel-inverted to yield the local density. However, when using a slit for one-dimensional imaging of a backlit target, the unique opacity of individual rays is lost. On the other hand, when measuring target self-emission, either a one-dimensional or a two-dimensional image can be Abel-inverted to yield the local emission. In fact, the two-dimensional Abel-inversion procedure described in the next section transforms the image to a one-dimensional image as would be seen by a slit. In this case the advantage of starting with a two-dimensional image is the ability to judge the symmetry and uniformity, whereas the advantage of using a spectrograph-slit combination is the ability to record a polychromatic image over a wide spectral range.

Abel Inversion

In the past, the problem of Abel inversion was studied mainly for a cylindrical geometry, where the data form a one-dimensional array perpendicular to the axis. For a spherical geometry, where the data form a two-dimensional array, the situation is different and merits some consideration. Figure 66.18 shows the geometry of the problem. In the case of a cylindrical source with its axis along the z axis, the observation is along the x direction and the measurements form a one-dimensional array along the y axis. The local parameter in terms of its line-of-sight integral is given by[4]

$$\varepsilon(R) = -(1/\pi)\int_{R}^{R_0} \left\{ \left[dF(y)/dy \right] \Big/ \left[y^2 - R^2 \right]^{1/2} \right\} dy, \qquad (1)$$

where R_0 is the radius of the cylinder, $\varepsilon(R)$ is the local quantity, and $F(y)$ is the measured integral of the same quantity along the line of sight. In spherical geometry, two-dimensional imaging forms an array in the y-z plane. Normally, only the results for

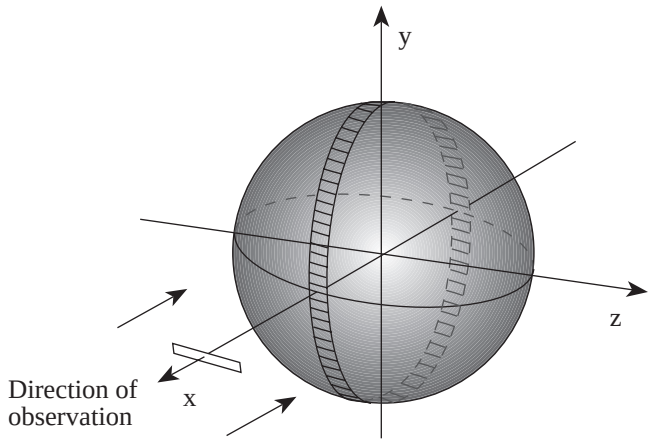

Figure 66.18
Geometry of the Abel inversion for backlighting a spherical source. Either two-dimensional monochromatic imaging (microscope-crystal combination) or one-dimensional polychromatic imaging (crystal-slit combination) can be used. To Abel-invert a two-dimensional image, the cylindrical solution can be applied to the coin-shaped element shown in the figure. Instead, the image can be integrated along the *z* axis and the solution for a spherical source viewed through a slit can be used.

$y = 0$ (or $z = 0$) are used, to which the cylindrical solution is applied.[5] To use the cylindrical solution while taking advantage of the entire two-dimensional data, we could average over the azimuthal angle (around the *x* axis), thereby converting the data into a one-dimensional array, and then use the cylindrical solution. Instead, we can integrate the data along, say, the *z* dimension. The solution of the Abel problem for the resulting one-dimensional array is the same as that for the case of imaging a sphere through a slit (in the *z* direction), namely[6]

$$\varepsilon(R) = (1/2\pi R)\left[dF(y)/dy\right]_{y=R}. \qquad (2)$$

The solution given by Eq. (2) is simpler than that given by Eq. (1) since it avoids the singularity at the lower bound of the integral (except at $R = 0$). In the case of imaged target emission, the numerical procedure described here is equivalent to using a one-dimensional imaging device, namely, an x-ray spectrograph with a slit for spatial resolution.

The Analyzed Test Case

A particular test case of a cryogenic target is studied using *LILAC* profiles and a radiation transport model (described in an earlier publication)[1] to simulate the two-dimensional backlighting image (including self-emission). The chosen pulse shape is typical of those to be used in high-performance implosions: its total duration is 9 ns; it rises slowly, then more rapidly, until reaching a plateau of 23 TW from 8 to 9 ns, then drops to zero. The total pulse energy is 30 kJ. The target is a 1060-μm-diam, 7.4-μm-thick CH shell containing a 90-μm-thick, cryogenic DT layer. Figure 66.19 shows the *LILAC* predictions for the temperature and density profiles at peak compression of this target (the electron and ion temperatures are nearly the same). Note the central hot spot surrounded by a cold and dense peripheral fuel region. By this time of the compression, the polymer shell and part of the fuel have been ablated away.

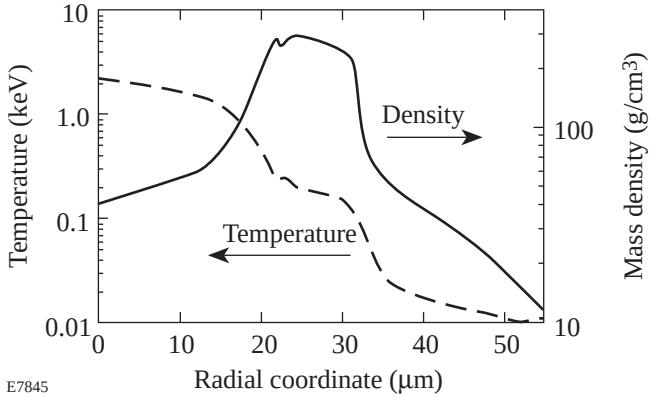

Figure 66.19
LILAC-computed temperature and density profiles of the cryogenic test implosion at peak compression.

Figure 66.20 shows a lineout through a two-dimensional image produced by backlighting and self-emission, at peak compression of the test target. The image is calculated assuming monochromatic detection of the $1s2p$–$1s^2$ line from a titanium backlighter ($\lambda = 2.62$ Å), using a diffracting crystal with a 4-eV bandpass. The curves are normalized to a spectral intensity of 7.0×10^{20} keV/(keV ns cm^2 Ω). This is the estimated intensity from a titanium backlighting target irradiated at 1.4×10^{15} W/cm^2 by a single OMEGA beam. The image in Fig. 66.20 can be divided into two sections: for radial distances greater than ~25 μm, the image is almost exclusively due to the backlighter; for radial distances less than ~25 μm, the image is almost exclusively due to self-emission. We treat Fig. 66.20 as a simulated experimental result and apply the same procedure as would be applied to an experimentally obtained image.

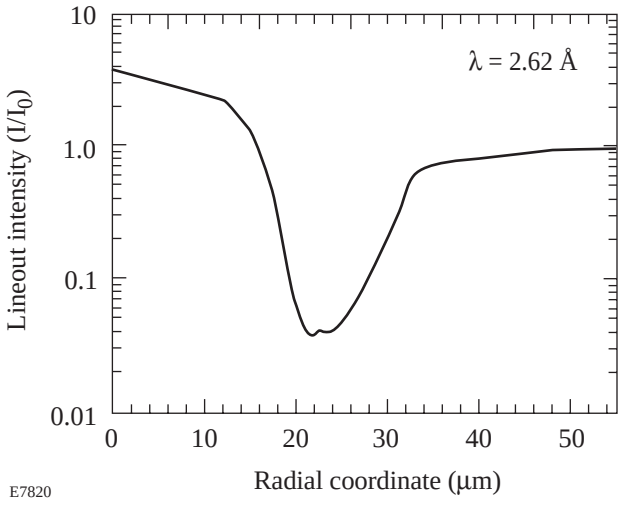

Figure 66.20
Lineout through the two-dimensional image due to backlighting and self-emission at peak compression of an imploded CH shell with cryogenic fuel. The image is calculated assuming monochromatic detection of the $1s2p$-$1s^2$ line of a titanium backlighter target ($\lambda = 2.62$ Å). The curves are normalized to a spectral intensity of 7.0×10^{20} keV/(keV ns cm^2 Ω).

Backlighting Image Analysis

The intensity $I(r)$ of the outer part of the image ($r > 25$ μm), where self-emission is negligible, directly yields the opacity along the line of sight, $\tau(r)$. Note that r stands for the radial coordinate in the two-dimensional image, as opposed to R, the radial coordinate in the three-dimensional target. The opacity is given by the relation $\tau(r) = \ln\left[I_0 / I(r)\right]$, where I_0 is the incident intensity of the backlighter. I_0 can be found from the intensity at larger radii where the backlighting radiation is essentially unattenuated, or from a separate laser shot where only the backlighter is irradiated. In a deuterium-tritium mixture, the absorption of x rays is due to inverse bremsstrahlung, and the opacity is given by[7]

$$\tau(r) = 2.334 \times 10^{-4}\left(\lambda^3 / T_c^{1/2}\right)\int_{x_2}^{x_1} \rho^2(r)\, dx, \qquad (3)$$

where λ is the wavelength in Å, T_c is the temperature in keV, ρ is the density in g/cm^3, and the integral is along the line of sight in the x direction: $x_1 = \left(R_0^2 - z^2 - y^2\right)^{1/2}$, $x_2 = -x_1$. By choosing a value for T_c, the electron temperature in the cold, absorbing fuel, Eq. (3) yields a two-dimensional array of the quantity ρ^2. We then integrate the array along the z axis and Abel-invert the results using Eq. (2). Figure 66.21 shows the density profiles obtained for three assumed temperatures of the absorbing region, compared to the original *LILAC* density profile used to obtain the image. As expected, the points for T_c = 0.2 keV agree with the *LILAC* curve in the region where the temperature is actually around 0.2 keV, and likewise for the other temperatures. Higher assumed temperatures result in higher densities because of the temperature and density dependencies in Eq. (3).

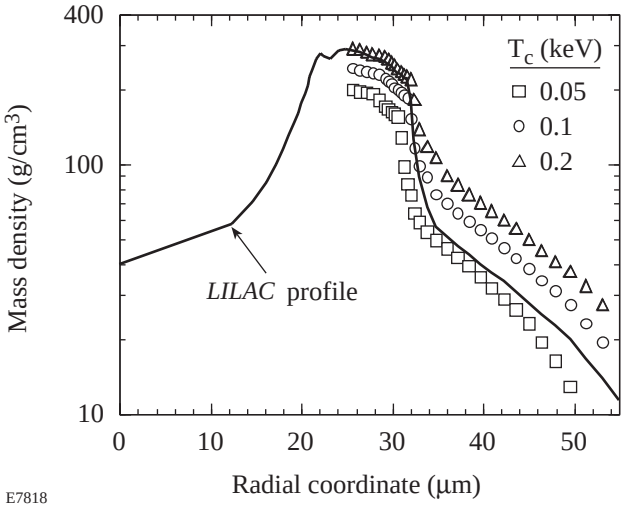

Figure 66.21
Abel-inverting the backlighting image of a cryogenic target (Fig. 66.20) yields the density distribution within the cold part of the compressed fuel for various assumed temperatures of the cold shell. The results are compared with the original *LILAC* density distribution (from Fig. 66.19) used in the simulation of the image.

Next, we convolve the image of Fig. 66.20 with the response function of the imaging device, which is assumed to be a Gaussian curve with FWHM of 10 μm. The Abel inversion was repeated, producing the results shown in Fig. 66.22. This analysis underestimates the peak density because the instrumental broadening reduces the depth of absorption in the backlighting image. Nevertheless, if the temperature is indeed between ~50 to 200 eV, the density profile in the cold region can be determined with an uncertainty of about a factor of 1.5. The effect of noise in the data will be discussed later.

The density determination can be extended to radii smaller than 25 μm if the self-emission component is subtracted from the image of Fig. 66.20. Since it is assumed that the backlighter emission is spectrally narrow, a slight wavelength detuning on the detector will create an image consisting of mostly the self-emission at a nearby wavelength, where the backlighter emission

is significantly reduced. In the case of 2-D imaging with a microscope-crystal combination,[3] this detuning can be achieved with an auxiliary crystal slightly off the Bragg angle.

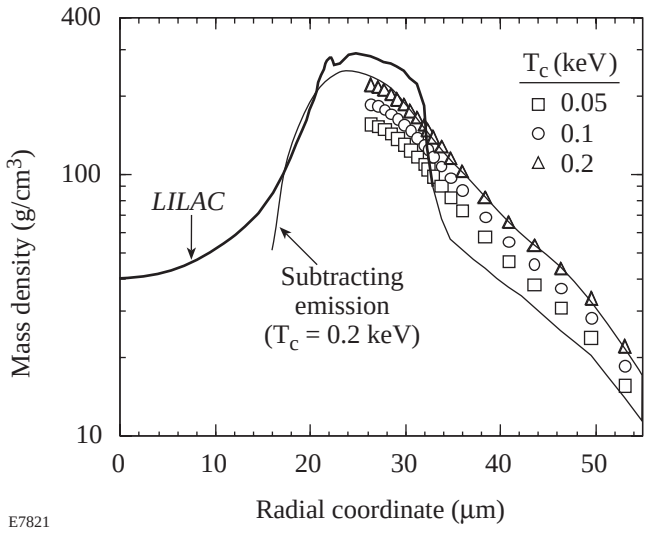

Figure 66.22
Same as Fig. 66.21, when the image of Fig. 66.20 is first convolved with an instrumental resolution curve of 10-μm FWHM and then Abel inverted. The thin curve, explained below, was obtained by Abel-inverting the image of Fig. 66.20, from which the self-emission contribution was first subtracted (the case $T = 0.2$ keV was assumed).

Using the radiation transport model,[1] the target emission image, at the backlighter wavelength (2.62 Å), was calculated and subtracted from the total image in Fig. 66.20, after each was convolved with a Gaussian instrumental profile of 10-μm FWHM. Finally, the Abel procedure was applied to the net backlighting image for the case of $T_c = 0.2$ keV. The result is shown by the thin curve in Fig. 66.22. Similar curves were obtained for other temperatures. It should be noted that most of the absorption occurs in the cold peripheral region, and it is the temperature of that region that is relevant. This is true even for the rays that traverse the target center. The thin curve in Fig. 66.22 does not extend all the way to the target center because of large errors in the Abel procedure at small radii. For an actual experiment, the procedure for extending the density curve would not be practical unless the relative emission intensity is lower than in the case shown in Fig. 66.20. This is because of the errors incurred in the subtraction of two comparable quantities (the total image and the self-emission component). A lower relative intensity of the target emission can arise from ineffective target compression or higher backlighting intensity.

Self-Emission Image Analysis

Information on the temperature in the central hot-spot region can be obtained from an Abel inversion of the emission profiles. To that end, images at a wide range of wavelengths are necessary. Such images can be readily obtained with a crystal spectrometer equipped with a spatially resolving slit. As explained earlier, one-dimensional slit images are suitable for the Abel inversion of self-emission. However, two-dimensional images are necessary in order to judge the symmetry and uniformity, and the usefulness of the one-dimensional data.

Figure 66.23 shows the model-simulated lineouts of continuum radiation images at various photon energies. The images contain the effect of radiation transport through the target layers. The effect of the cold, annular fuel region is evident by the severe attenuation of radiation below ~5 keV.

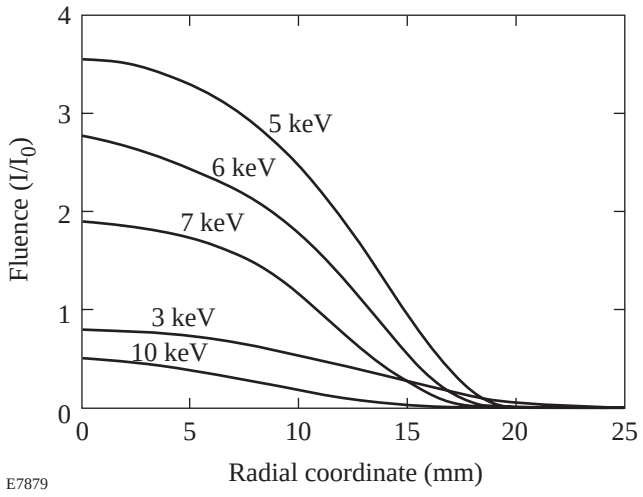

Figure 66.23
Spatial profiles of the emission continuum calculated by the model.[1] The radial coordinate is in the plane of the image (i.e., it is the distance of the line-of-sight from one going through the center of the target). The curves represent the emergent spectra; i.e., they include the attenuation by the cold shell. The normalization intensity I_0, as in Fig. 66.20, equals 7.0×10^{20} keV/(keV ns cm^2 Ω).

We first study the information contained in space-integrated spectra. Figure 66.24 shows a comparison between the time-integrated and space-integrated continuum spectrum calculated by *LILAC* and the peak-compression spectrum calculated by spatially integrating the curves in Fig. 66.23. The comparison serves to show consistency between the two calculations. The difference at the softer end of the spectrum is due to emission before peak compression, from the outer target

layers. Note that since the emission of the compressed core lasts for about 1 ns, the two curves at high energies are comparable. The comparison also shows that the peak temperature of the hot spot can be determined by a time-integrating spectrograph if a sufficiently high-energy part of the spectrum is used to measure the slope. Since the temperatures T_h deduced in Fig. 66.24 are close to the peak temperature in the test implosion (see Fig. 66.19), we conclude that the peak core temperature can be experimentally determined from a spectrograph that integrates the emission in both time and space.

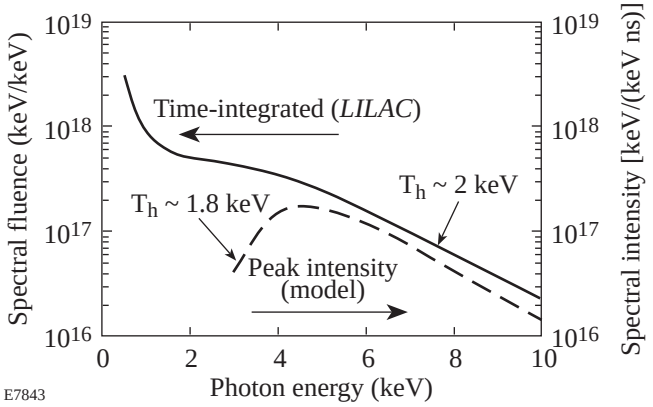

Figure 66.24
Computed continuum spectrum calculated by *LILAC* (time integrated) and by the model described here (at peak compression). Both are integrated over the volume of the target. The curves represent the emergent spectra; i.e., they include the attenuation by the cold shell. The slopes yield the hot-spot temperature T_h.

The ability to measure the core temperature using the high-energy end of the spectrum, where shell attenuation is small, has been recognized previously.[8] However, since the backlighting image provides a measure of the shell attenuation, we can correct for it and extend the usefulness of the continuum to lower photon energies, where the intensity is higher, thus yielding a better signal-to-noise ratio. Figure 66.25 shows the results of such a procedure. For various choices of the shell temperature, the corresponding density profile from Fig. 66.22 was used to calculate the opacity τ_0 along the radial direction, and the lower curve of Fig. 66.25 was then multiplied by $\exp(\tau_0)$. As expected, the resulting curve is a single exponential with the same slope as that of the high-energy part of the emergent spectrum. It is not surprising that the various choices of cold-region temperatures result in the same curve: the points on this curve were obtained from the density profiles of Fig. 66.22 and the corresponding temperatures, all of which were derived from the same backlighting image, thus the same opacity. In simple terms, the opacity correction can be approximately derived directly from the backlighting image, without knowing the density or the temperature.

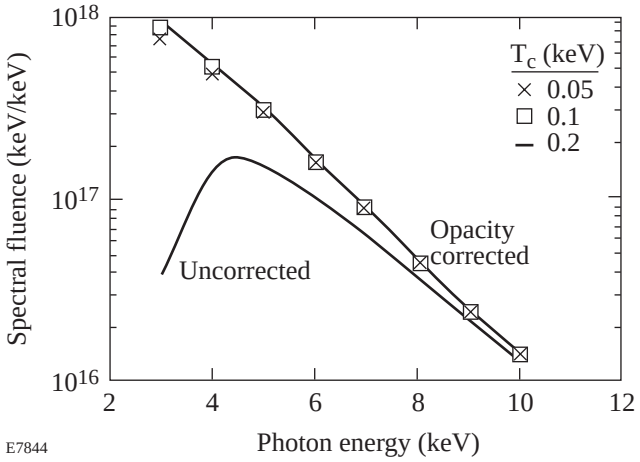

Figure 66.25
Lower curve: model-computed continuum at peak compression (from Fig. 66.24); upper curve and points: the spectrum corrected for absorption by the cold-fuel shell. The results assumed that cold-shell temperatures essentially coincide.

In addition to determining the peak temperature, the spatial temperature profile within the hot spot can be studied as well. To perform this analysis, we begin by simulating another experimental observation. The spectrum at different locations within the hot spot can be calculated from the emergent profiles, such as in Fig. 66.23. Such profiles must be integrated to simulate one-dimensional slit images, then convolved with an instrumental resolution curve (again assumed to be a Gaussian of 10-μm FWHM) and then corrected for the attenuation by the cold shell. We then apply the Abel inversion according to Eq. (2). Two points need to be addressed: (a) This procedure is valid only if the opacity within the hot spot itself is negligible, and (b) the radial opacity τ_0 must be replaced with an opacity calculated (from Eq. 3) separately along each line of sight. Using the profiles in Fig. 66.19 we calculate the opacity of the hot region to be ~0.03 and thus negligible; this is expected because of both the low density and high temperature of this region.

Figure 66.26 shows the resulting spectra at several locations within the hot spot. The unit of local emission (or emissivity) ε_0 is related to the unit of emergent intensity I_0 of Figs. 66.20 and 66.23, i.e., $\varepsilon_0 = 7.0 \times 10^{20}$ keV/(keV ns cm^3 Ω). As expected, the curves each correspond to a well-defined temperature. Finally, the inferred temperature profile

is shown in Fig. 66.27, compared with the *LILAC*-calculated profile from Fig. 66.19. The general agreement between the two curves is expected and provides a check of consistency in the calculations. However, the deviation at the periphery of the hot spot shows the effect of finite spatial resolution. The slit transfers intensity to the lower-intensity parts of the image; since this intensity has a more-pronounced effect on the hardest and weakest parts of the spectrum, the result is a rise in the apparent temperature.

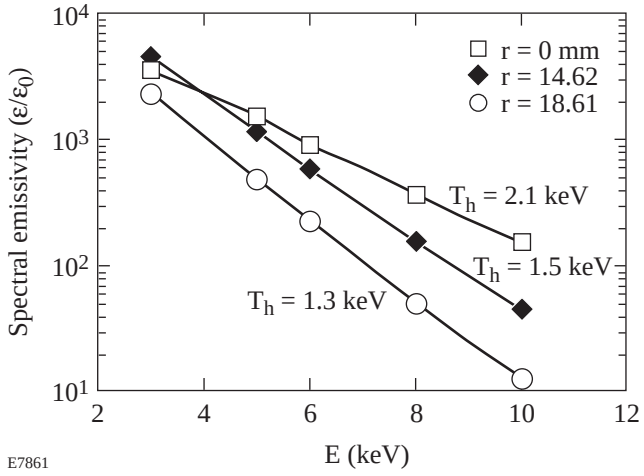

Figure 66.26
Continuum spectra of the emission at various core locations. The emergent profiles of Fig. 66.23 have been integrated to simulate one-dimensional slit images, then convolved with an instrumental resolution curve (assumed to be a Gaussian of 10-μm FWHM), and Abel-inverted according to Eq. (2). The absorption by the cold fuel shell has been accounted for (before Abel-inverting). The emissivity unit is $\varepsilon_0 = 7.0 \times 10^{20}$ keV/(keV ns cm^3 Ω).

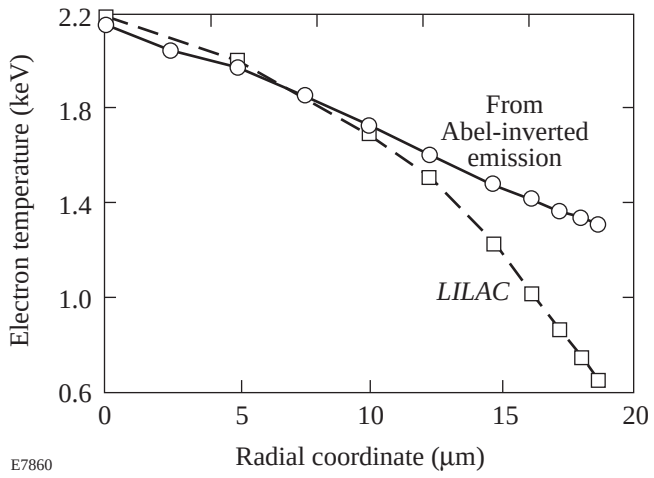

Figure 66.27
Temperature profile in the hot spot, from Fig. 66.26, compared with the *LILAC*-calculated profile at peak compression.

Effect of Noise in the Data

The foregoing analysis has effectively assumed that the data subjected to the Abel inversion is devoid of noise. Starting with the image in Fig. 66.20, we will now study how noise in the measured data affects the inverted results. After convolution with an instrumental broadening curve of 10-μm FWHM, random noise (±25%) is added to the signal and the Abel procedure (assuming T_c = 0.2 keV) is repeated many times. Because the Abel inversion involves a derivative over space [(see Eq. (2)], the data normally has to be smoothed. We apply a 5-point smoothing procedure to the intensity profiles before Abel inverting. This is a mild smoothing since the smoothing range extends over only ~10% of the total range of the image. Figure 66.28 shows several examples of the resulting mass-density profile, compared to the profile with no noise. The error in the mass density increases with the radial coordinate: it is ~15% at $r = 25$ μm and increases to >50% for $r > 45$ μm. This increase is related to the dependence of the opacity τ on the image intensity I. Since $\tau = \ln(I_0/I)$, the relative error in the opacity is related to the relative error in the measured intensity according to $(\Delta\tau/\tau)/(\Delta I/I) = [\ln(I_0/I)]^{0.5}$. Thus, the error in the opacity (and hence in the mass density) increases sharply at large radii, where the opacity is small. However, the error in the mass density is still for the most part smaller than the error due to the uncertainty in the value of T_c. Thus, the latter will determine the total error, especially if the noise in the experimental data is kept below ±25%.

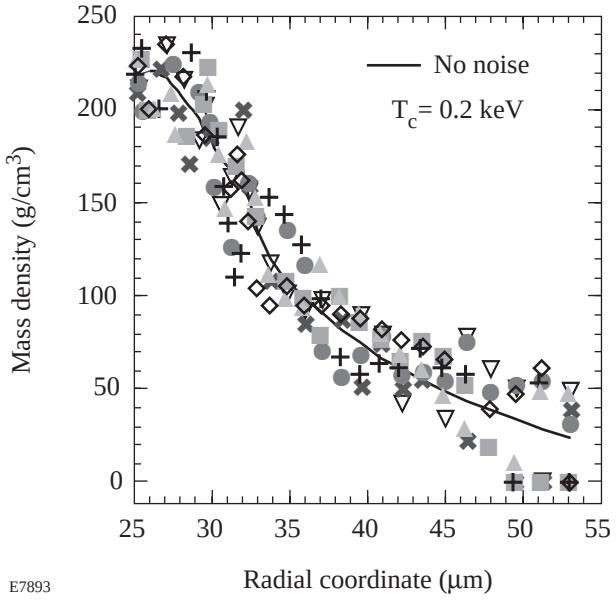

Figure 66.28
Effect of ±25% random noise in the backlighting image on the mass-density profile obtained from Abel inversion. Instrumental resolution of 10-μm FWHM was included.

The same procedure was applied to the emission profiles of Fig. 66.23: after converting these profiles to slit images and accounting for instrumental broadening, a ±25% random noise was added to the points. Then the effect of attenuation by the cold shell was accounted for, and finally the Abel inversion was applied to yield the local spectral emission. Figure 66.29 shows a sample of random noise runs. The error in the local emission increases with the radius up to ±15% for $r = 0$ because, when the profile does not increase toward the center, the Abel inversion essentially involves the subtraction of two almost identical quantities. The resulting temperature at $r = 0$ varies in the range of 2.0 to 2.3 keV, and the variation is even smaller for larger radii. Thus, a ±25% noise in the experimental image results in a relatively small error in the temperature, especially for larger radii, where, conversely, instrumental resolution strongly affects the results (see Fig. 66.27).

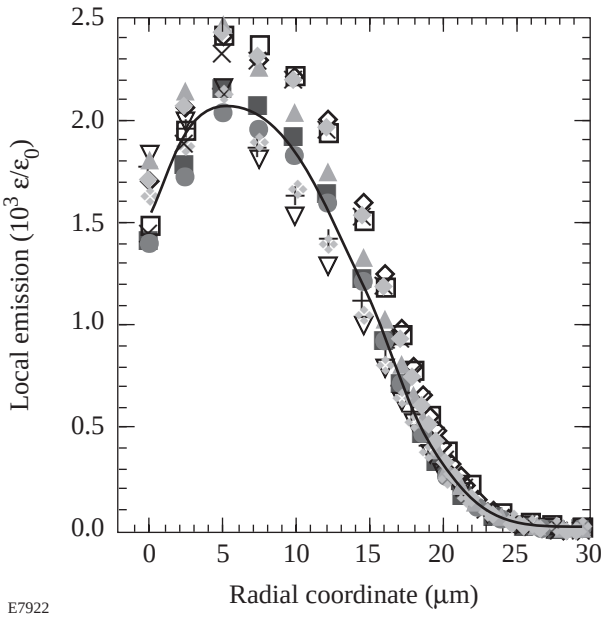

Figure 66.29
Effect of ±25% random noise in the self-emission image on the local emission profile obtained from Abel inversion. Instrumental resolution (of a slit) of 10-μm FWHM was included. The resulting errors in the temperature profile are less than ±10%.

Conclusion

The Abel inversion can greatly enhance the usefulness of either emission or backlit images of imploded targets. The measurement of only the emission from a cryogenic target is of limited value. The deduction of the hot-spot temperature is compromised by not knowing the attenuation through the cold shell. To overcome this difficulty, the spectrum has to be measured at sufficiently high photon energies, where the intensity is low. Likewise, imaging the emission can yield the hot-spot size, but without information on the existence of a cold annular region, the very existence of a hot spot is uncertain. On the other hand, two-dimensional monochromatic backlighting imaging supplemented by one-dimensional polychromatic imaging can yield significant additional information: the former can yield the density distribution within the cold, dense shell, and the latter can yield the temperature distribution within the hot spot. To achieve this, a spatial resolution of ~10 μm in both instruments is required.

ACKNOWLEDGMENT

This work was supported by the U.S. Department of Energy Office of Inertial Confinement Fusion under Cooperative Agreement No. DE-FC03-92SF19460, the University of Rochester, and the New York State Energy Research and Development Authority. The support of DOE does not constitute an endorsement by DOE of the views expressed in this article.

REFERENCES

1. Laboratory for Laser Energetics LLE Review **58**, NTIS document No. DOE/SF/19460-17, 1994 (unpublished), p. 57.
2. B. Yaakobi, F. J. Marshall, Q. Su, and R. Epstein, J. X-Ray Sci. Technol. **5**, 73 (1995).
3. F. J. Marshall and Q. Su, Rev. Sci. Instrum. **66**, 725 (1995); Laboratory for Laser Energetics LLE Review 66, NTIS document No. DOE/SF/19460-125, 1996 (unpublished), p. 60 (this issue).
4. K. Bockasten, J. Opt. Soc. Am. **51**, 943 (1961).
5. N. A. Magnitskii and S. A. Magnitskii, Sov. J. Quantum Electron. **7**, 441 (1977).
6. C. M. Vest and D. G. Steel, Opt. Lett. **3**, 54 (1978).
7. B. Yaakobi, R. Epstein, and F. J. Marshall, Phys. Rev. A **44**, 8429 (1991).
8. F. J. Marshall, J. A. Delettrez, R. Epstein, and B. Yaakobi, Phys. Rev. E **49**, 4381 (1994).